

Article

Optical and Superhydrophilic Characteristics of TiO₂ Coating with Subwavelength Surface Structure Consisting of Spherical Nanoparticle Aggregates

Yuki Kameya *  and Hiroki Yabe

Department of Mechanical Engineering, Chiba Institute of Technology, Chiba 275-0016, Japan

* Correspondence: yuki.kameya@it-chiba.ac.jp or yuki.kameya.jp@gmail.com; Tel.: +81-47-478-0265

Received: 17 August 2019; Accepted: 24 August 2019; Published: 26 August 2019



Abstract: It is expected that the applications of photocatalytic coatings will continue to extend into many areas, so it is important to explore their potential for enhanced functionality and design flexibility. In this study, we investigated the effect of a subwavelength surface structure in a TiO₂ coating on its optical and superhydrophilic characteristics. Using submicron-scale spherical aggregates of TiO₂ nanoparticles, we fabricated a TiO₂ film with a subwavelength surface structure. Optical examination showed the enhanced transmittance of visible light compared to that of a plain surface. This was considered to be a result of a graded refractive index at the air–TiO₂ interface. The effect of the subwavelength surface structure on optical transmittance was also demonstrated by the numerical simulation of visible light propagation in which Maxwell’s equations were solved using the finite-difference time-domain method. In addition, superhydrophilic behavior without ultraviolet light illumination was observed for the subwavelength-structure film via the measurement of the contact angle of a water drop. Furthermore, it was confirmed that the photocatalytic activity of the proposed film was comparable with that of a standard TiO₂ film. It was suggested that the control of the subwavelength surface structure of a TiO₂ film could be utilized to achieve novel properties of photocatalytic coatings.

Keywords: photocatalyst; TiO₂; nanoparticle; subwavelength surface structure; superhydrophilicity

1. Introduction

Titanium dioxide (TiO₂) has been widely used to decompose pollutants via photocatalytic reactions [1,2] and to control surface wettability for self-cleaning coatings [3]. Because TiO₂ has a high refractive index ($n \sim 2.6$ [4]) and no absorption band in the visible wavelengths, surface coatings of TiO₂ appear white. This intrinsic property limits the color design flexibility of TiO₂ coatings. Moreover, although TiO₂ is known to exhibit superhydrophilicity when illuminated with ultra-violet (UV) light, an external source of UV light is necessary to utilize its superhydrophilic function [3,5]. Therefore, it is desirable to develop TiO₂ films that provide enhanced transparency and superhydrophilicity without the need for UV-light irradiation.

To improve visible-light transmission at optical interfaces, one possible approach is to fabricate anti-reflection surface structures. A subwavelength surface pattern that enables an optical interface to have a graded refractive index which reduces light reflection [6]. Such surfaces are called moth-eye anti-reflective structures [7]. Considering this anti-reflection mechanism, it should be possible to increase the transparency of a TiO₂ film by fabricating a film with such subwavelength surface structures (i.e., structures having characteristic dimensions less than visible-light wavelengths).

Furthermore, the surface roughness of a hydrophilic material is known to enhance its apparent hydrophilicity [8]. Because TiO_2 is intrinsically hydrophilic, a textured surface on the TiO_2 film has the potential to provide increased hydrophilicity.

On the basis of the above considerations, it is expected to control the microscale surface structure of the TiO_2 film to achieve favorable optical and wetting characteristics. Recently, TiO_2 spherical nanoparticle aggregate (NSA) was developed [9]. The diameter of NSA is 100–200 nm, and, therefore, the top layer of a packed NSA film cannot be a plain surface but has an intrinsic subwavelength surface structure (Figure 1). Because such films consist of TiO_2 nanoparticles, they also have porous structures. A porous TiO_2 structure allows gas molecules to diffuse into the film, which results in the effective production of radicals before photo-excited carriers are lost [1]. Consequently, an NSA film is considered to show improved optical and wetting characteristics without the degradation of its photocatalytic function.

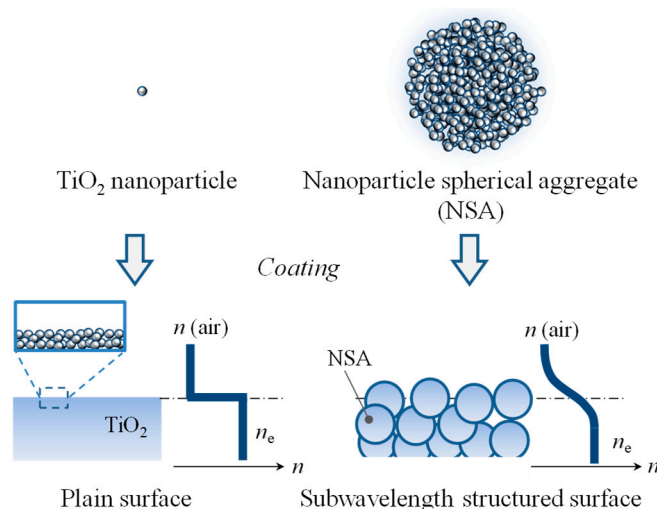


Figure 1. Illustration of a graded refractive index at the air– TiO_2 interface using a spherical nanoparticle aggregate (NSA) film.

In this work, we investigated the effect of the subwavelength surface structure of a TiO_2 coating on its optical and superhydrophilic characteristics. Using submicron-scale TiO_2 NSAs, we fabricated a TiO_2 film with a subwavelength surface structure. Visible-light transmittance was measured to examine the optical property resulting from the graded refractive index at the air– TiO_2 interface. The effect of the surface structure on the visible-light transmittance was also demonstrated by the numerical simulation of light propagation in which Maxwell’s equations were solved using the finite-difference time-domain method. In addition, we performed water-drop contact-angle measurements to demonstrate superhydrophilic behavior without UV-light illumination. Finally, we confirmed the photocatalytic activity of an NSA film.

2. Experimental

2.1. TiO_2 Film Samples

We prepared TiO_2 aqueous dispersions using two kinds of TiO_2 particles: NSA (Ujiden Chemical, Kochi, Japan) and AEROXIDE® P25 (Evonik Industries, Essen, Germany). P25 is a fine powder of nanoparticles with mean diameter of about 21 nm. It was used as a standard TiO_2 material to evaluate the properties of NSA. To break large agglomerates in each dispersion, ultrasonication was performed using an UH-50 ultrasonic homogenizer (SMT, Kanagawa, Japan). A glass substrate was treated with Ar plasma to clean the surface and enhance its wettability. A specified amount of dispersion was dropped on the glass substrate and spontaneously spread over the surface. We managed to apply it to

uniformly cover the substrate surface. After being dried at room temperature, samples were heated at 600 °C for 20 min to sinter the particles [10].

The prepared samples were observed using a scanning electron microscope (SEM) S-4700 (Hitachi, Tokyo, Japan). The glass plate caused surface charging during SEM observation; therefore, we coated the samples with osmium using a Neoc coater (Meiwafosis, Tokyo, Japan).

2.2. Optical Measurement

The optical transmittance of each sample was measured using a flame spectrometer with a halogen light source (Ocean Optics, Dunedin, FL, USA). A diffraction grating was used to split the light, and the intensity of each component was detected by a silicon CCD array. The measurement was performed for wavelengths in the range of 0.4–0.9 μm. The normal spectral transmittance was determined.

2.3. Water Contact Angle Measurement

To evaluate the wetting behavior, we measured the water contact angle at the surface. A water droplet (5 μL) was applied to the sample surface, and a side-view photo image was captured using a CMOS camera (3R-MSUSB401, 3R Solution, Fukuoka, Japan). Then, the obtained imaged was analyzed to determine the contact angle [11].

2.4. Photocatalytic Performance Evaluation

Methylene blue (MB) decomposition was used to evaluate the photocatalytic activity of prepared samples. We deposited an aqueous solution of MB on a TiO₂ film samples. We used a near-ultra-violet (NUV) lamp (FPL27BLB, Sankyo Denki, Kanagawa, Japan). The light intensity was about 4 mW/cm², which was measured using a UV light meter (UV-340C, Custom, Tokyo, Japan). Because MB has an optical absorption band in visible wavelengths, the change of optical transmittance was measured for three hours to evaluate the progress of MB decomposition.

3. Numerical Simulation

To investigate the effects of the surface subwavelength microstructure of a TiO₂ coating on the transmittance of visible light, we performed a numerical simulation of visible-light propagation through a textured surface. Maxwell's equations were solved using the finite-difference time-domain (FDTD) method [12]. We assumed optical properties and geometry to model the air–TiO₂ interface of the NSA film, as described below.

Because NSA consists of sintered nanoparticles, it has a fine porous structure. To evaluate the refractive index of the porous medium, we introduced the effective refractive index n_e , calculated from the Bruggeman effective medium approximation [13]:

$$f_1 \frac{(n_1^2 - n_e^2)}{(n_1^2 + 2n_e^2)} + f_2 \frac{(n_2^2 - n_e^2)}{(n_2^2 + 2n_e^2)} = 0 \quad (1)$$

where f is the volume fraction and the subscripts 1 and 2 refer to air and TiO₂, respectively, in the present case. For the substrates before sintering, we assumed that the porosity was 0.4 (random packing of spheres [1]), so $f_1 = 0.4$ and $f_2 = 0.6$. When we considered $n_1 = 1$ and $n_2 = 2.6$ [4], we obtained $n_e = 1.93$. Therefore, we used $n_e = 1.93$ as the effective refractive index of NSA in the present numerical simulation.

Then we modeled the subwavelength surface structure of the NSA film. The model geometry for the simulation is schematically shown in Figure 2a. Because of the spherical structure of each NSA, we assumed a convex surface pattern. The volume fraction of NSA at the air–TiO₂ interface varied along the surface-normal direction (i.e., the x direction); hence, a graded refractive index was achieved as illustrated in Figure 1. To examine the influence of the graded refractive index on the visible light transmission, we made several geometries, as shown in Figure 2b. We defined the aspect

ratio of each convex structure as the height h divided by the width w . A parabolic function was used to create convex interface patterns with various aspect ratios. Because our NSA sample had a range of diameters, we used $w = 0.1$ and $0.2 \mu\text{m}$, and the aspect ratio was varied from 0 to 0.5. Hence the height h of each convex structure is equal to the peak x value appearing at $z = 0.05$ and $0.1 \mu\text{m}$ for $w = 0.1$ and $0.2 \mu\text{m}$, respectively. The aspect ratio of 0 corresponds to a plain interface.

Because we used a periodic concave pattern to model the air–TiO₂ interface, the periodic boundary condition was used in the z direction (Figure 2a). For the x direction, we used the anisotropic perfectly matched layer (APML) absorbing boundary conditions [12]. The simulation region ($x \times z$) was $6 \mu\text{m} \times 0.2 \mu\text{m}$ with the mesh size $\Delta x = \Delta z = 5 \text{ nm}$. A monochromatic plane wave of $0.55 \mu\text{m}$ wavelength, which is in the middle of visible range, was used to evaluate the transmittance of visible light. We investigated the influence of aspect ratio on the transmittance. As a solver, we used the commercial software OptiFDTD version 12 (Optiwave Systems) [14].

To confirm the validity of our simulation and subsequent data processing, we numerically calculated the normal transmittance of visible light ($\lambda = 0.55 \mu\text{m}$) regarding a plain TiO₂ layer and compared the result with the analytical solution of Maxwell's equations. The transmission coefficient τ at the air–TiO₂ interface is given as [15]:

$$\tau = \frac{4 n_1 n_e}{(n_1 + n_e)^2} \quad (2)$$

It should be noted that the transmittance T determined in the optical measurement has physical meaning different from the transmission coefficient τ ; T includes the effect of multiple reflections at several interfaces in the sample, while τ is determined only by the phenomenon at the air–TiO₂ interface.

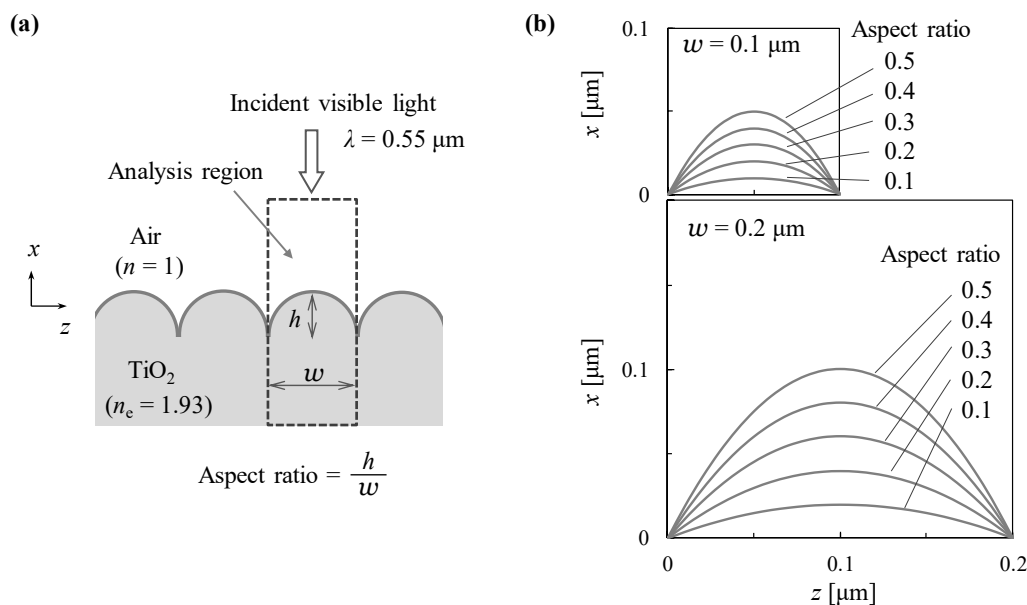


Figure 2. Numerical simulation model: (a) Analysis region. (b) Model geometries with various aspect ratios.

4. Results and Discussion

4.1. Visible-Light Transmittance

First, we visually examined the NSA film by comparing it with the P25 film. We prepared the dispersions of NSA and P25 with 30 wt % solid content, and each dispersion was coated onto black paper (Figure 3a). It is clear that the color change (i.e., black to white) observed in the P25-coated area

was greater than that in the NSA-coated area. This result suggests that the visible light scattering by the NSA-coated surface was weaker than that from the P25-coated surface.

To confirm quantitatively the difference between the NSA and P25 films in terms of optical property, we measured the transmittance of TiO₂-coated samples in the visible wavelength range. The dispersion of NSA or P25 with 5 wt % solid content was used to make film on a glass substrate for each sample. Then, the normal spectral transmittance of each sample was measured. The results are shown in Figure 3b. The transmittance of the NSA film is higher than that of P25 in the visible wavelengths. For example, the result at the wavelength of 0.55 μm showed $T = 62\%$ and 51% for NSA and P25, respectively, so the difference between these films was significant. The obtained results are in accordance with the above-mentioned visual examination using black paper.

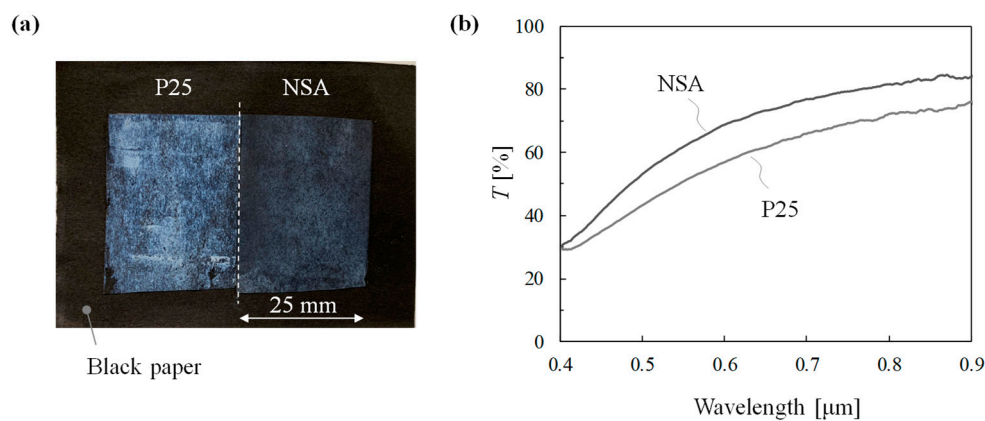


Figure 3. (a) Photograph of a coating surface on black paper. (b) Spectral transmittance in the visible wavelength range.

4.2. SEM Observation

The TiO₂ film samples used in the optical transmission measurement were observed using SEM. The obtained top-view images are shown in Figure 4. The P25 film had no unique geometrical features (Figure 4a), and the surface roughness that existed was possibly due to the agglomeration of particles during the process of drying the dispersion [16]. Concerning the NSA film (Figure 4b), the spherical shape of NSA remained even after the sintering process. As expected, the surface structure of each film reflected the basic-unit size of particles, i.e., the primary-particle diameter of about 21 nm for P25 and the aggregate diameter of 100–200 nm for NSA. We confirmed a remarkable difference in the qualitative characteristics of surface structures between the two samples. Hence, we proceeded to the numerical simulation of visible light transmission to explain the observed difference in the transmittance.

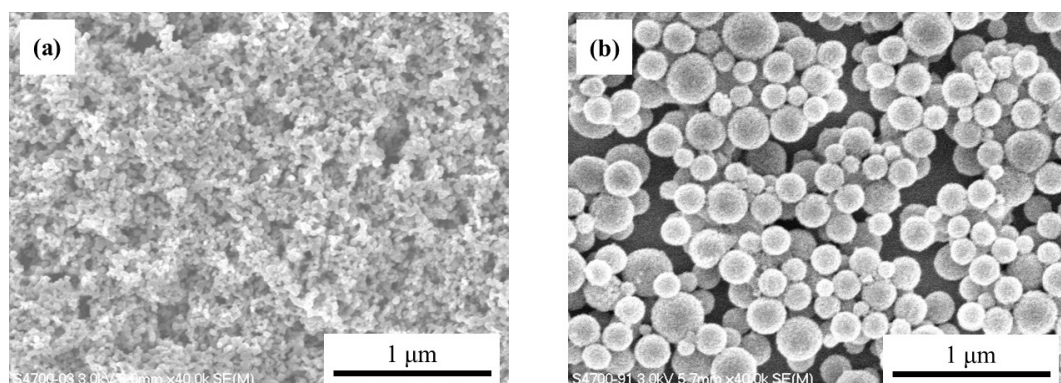


Figure 4. Top-view SEM images: (a) P25 and (b) NSA.

4.3. Numerical Simulation of Visible-Light Transmission

The transmission coefficient τ at the air–TiO₂ interface was numerically calculated for each geometry described in Section 2 (Figure 2b). The simulation results are summarized in Figure 5. The transmission coefficients τ are plotted against the aspect ratio of a concave surface structure. The circle and triangle symbols show results of $w = 0.1$ and $0.2 \mu\text{m}$, respectively.

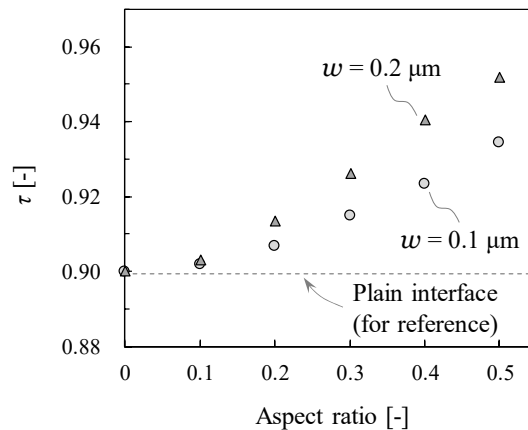


Figure 5. Simulated transmission coefficient as a function of aspect ratio (circles: $w = 0.1 \mu\text{m}$, and triangles: $w = 0.2 \mu\text{m}$). A value corresponding to the transmission coefficient of a plain interface is indicated by the horizontal dashed line for reference.

The case in which the aspect ratio was zero corresponds to a plain interface, so the predicted τ values for two results ($w = 0.1$ and $0.2 \mu\text{m}$) should be the same value. Using Equation (2), the transmission coefficient obtained for a plain interface was 0.899. Therefore, the validity of our numerical simulation model and subsequent data processing was confirmed.

As the aspect ratio increased, the transmission coefficient showed higher values. This trend is in accordance with our expectation because the effect of a graded refractive index at the air–TiO₂ interface is emphasized at higher aspect ratios.

The difference between the cases of $w = 0.1$ and $0.2 \mu\text{m}$ can be also interpreted as indicating spatial variation of the refractive index. The volume fraction of a convex structure for the aspect ratio of 0.5 is plotted against the x coordinate (i.e., surface normal direction) in Figure 6. We found that the gradient of the curve for $w = 0.2 \mu\text{m}$ was lower than that for $w = 0.1 \mu\text{m}$. The lower gradient of the curve means spatially broader distribution of the refractive index, which results in transmission enhancement.

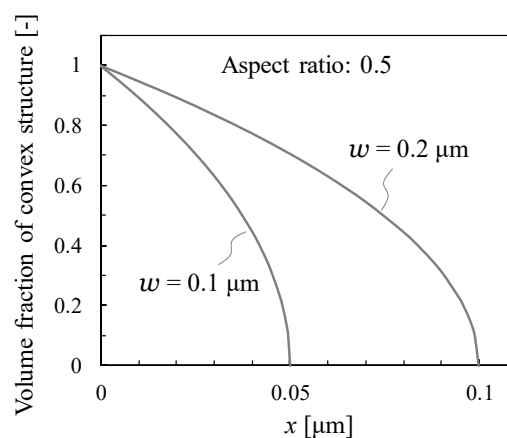


Figure 6. Volume fraction of a convex structure with surface normal (x -axis) direction.

On the basis of these simulation results, we expect an NSA film with a subwavelength surface structure should show improved transparency. Considering the increasing transmission coefficient with the aspect ratio, there is potential for improvement by modifying the surface structure of the NSA film.

4.4. Wetting

Wettability is an important property of coatings intended to achieve a self-cleaning surface. To evaluate the water wettability of our TiO₂ samples, we performed contact angle measurement. The photo images taken to determine the contact angle θ_c are shown in Figure 7. To emphasize the change in the contact angle for the TiO₂ coating, we also used a glass slide that was exposed to air and not coated with TiO₂. The uncoated glass had $\theta_c = 34^\circ$, which is not an ideal result for a clean glass surface but a practical result for a glass surface exposed to airborne contaminants (Figure 7a). For the P25-coated surface, a drop of water readily spread over the surface and eventually showed $\theta_c < 10^\circ$, which is a characteristic of superhydrophilic surfaces (Figure 7b). The NSA-coated surface also exhibited superhydrophilic behavior (Figure 7c). Additionally, a sessile-drop technique is often used to distinguish advancing and receding contact angles [17,18]. Because a water drop was simply deposited on each sample in the present experiments, the results are close to advancing contact angles.

Even though we did not use UV light irradiation in these experiments, we observed superhydrophilic behavior for both the P25 and NSA coatings. We consider that the surface roughness influenced the small contact angle. The TiO₂ coatings, not only with NSA, but also with P25, exhibited surface roughness. Even though their scales and features were totally different, it is considered that the roughness of both films was sufficient to enhance their water wetting property; this consideration can be supported by the observation indicating that nanoscale roughness affects surface wetting [19].

Because it is difficult to accurately measure very small contact angles ($\theta_c < 10^\circ$), we were not able to determine the difference in wettability of the P25 and NSA coatings in the present experiments. To quantitatively investigate the difference in the degree of superhydrophilicity, a special experimental setup is needed [20]. Future work is necessary to optimize the surface microstructure proposed here.

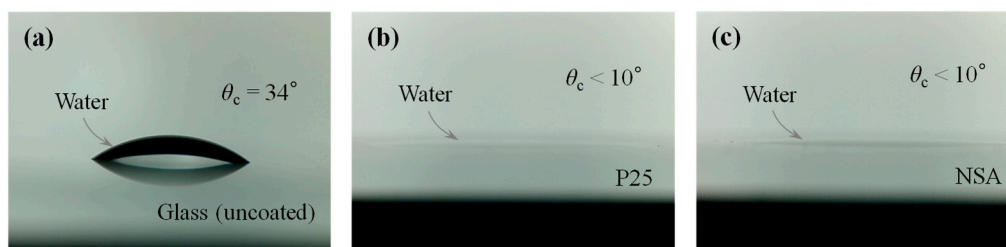


Figure 7. Contact angle measurement: (a) Uncoated glass, (b) P25 film, and (c) NSA film.

4.5. Photocatalytic Decomposition of MB

To demonstrate the photocatalytic performance of the NSA-coated film, we conducted MB decomposition experiments. After depositing MB on the NSA and P25 films, we measured their visible-light transmittance to evaluate the amount of MB on the samples. Then, we started to irradiate them with UV light to enhance the photocatalytic decomposition of MB. We measured the visible-light transmittance every hour.

The results are shown in Figure 8. At the beginning (the time was 0 h), the transmittance of the NSA film was higher than that of the P25 film because of the difference in their clean conditions (shown in Figure 3b). As the reaction proceeded, the transmittance of each sample increased due to decomposition of light-absorbing MB. The temporal change of transmittance indicates the photocatalytic reaction rate of MB decomposition. Because the slope of transmittance was similar for each sample, we can assume there was no remarkable difference in the MB decomposition rates. In this way, we confirmed that the NSA film had photocatalytic performance comparable to that of a typical film with the TiO₂ coating

using P25. Therefore, we expect to be able to utilize the useful features of NSA films without reducing their photocatalytic activity.

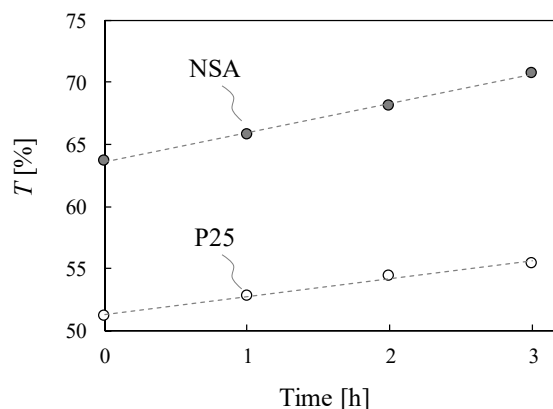


Figure 8. Transmittance variation with time during photocatalytic methylene blue (MB) decomposition.

5. Conclusions

We investigated the effect of a subwavelength surface structure of a TiO₂ coating on its optical and superhydrophilic characteristics. Using submicron-scale TiO₂ NSA, we fabricated a TiO₂ film with a subwavelength surface structure. Optical examination showed an enhanced transmittance of visible light compared to that of a plain surface, which was considered to be a result of a graded refractive index at the air–TiO₂ interface. The numerical simulation supported the improved transparency. In addition, superhydrophilic behavior without ultraviolet-light illumination was observed for the subwavelength-structured film via the contact angle measurement of a water drop. It is suggested that we can utilize the favorable features of an NSA film, such as greater visible-light transmission and superhydrophilicity, without degrading its photocatalytic performance. Using a subwavelength surface structure on a photocatalytic film appears to influence its useful features, so it is hoped to further investigate the potential for surface design of photocatalytic coatings.

Author Contributions: Conceptualization, Y.K.; Methodology, Y.K.; Formal Analysis, Y.K. and H.Y.; Investigation, Y.K. and H.Y.; Writing—Review and Editing, Y.K.

Funding: This research received no external funding.

Acknowledgments: The authors thank Tomohiro Okazoe of Ujiden Chemical Industry for supplying the TiO₂ materials and useful suggestions. A part of the experiments and numerical simulation were conducted by Takahiro Yamada and Daiki Sato as an undergraduate research program of Chiba Institute of Technology.

Conflicts of Interest: The authors declare no conflicts of interest.

References

1. Kameya, Y.; Torii, K.; Hirai, S.; Kaviany, M. Photocatalytic soot oxidation on TiO₂ microstructured substrate. *Chem. Eng. J.* **2017**, *327*, 831–837. [[CrossRef](#)]
2. Truppi, A.; Luna, M.; Petronella, F.; Falcicchio, A.; Giannini, C.; Comparelli, R.; Mosquera, M.J. Photocatalytic activity of TiO₂/AuNRs-SiO₂ nanocomposites applied to building materials. *Coatings* **2018**, *8*, 296. [[CrossRef](#)]
3. Banerjee, S.; Dionysiou, D.D.; Pillai, S.C. Self-cleaning applications of TiO₂ by photo-induced hydrophilicity and photocatalysis. *Appl. Catal. B Environ.* **2015**, *176*, 396–428. [[CrossRef](#)]
4. Chen, T.L.; Hirose, Y.; Hitosugi, T.; Hasegawa, T. One unit-cell seed layer induced epitaxial growth of heavily nitrogen doped anatase TiO₂ films. *J. Phys. D Appl. Phys.* **2008**, *41*, 062005. [[CrossRef](#)]
5. Wang, R.; Hashimoto, K.; Fujishima, A.; Chikuni, M.; Kojima, E.; Kitamura, A.; Shimohigoshi, M.; Watanabe, T. Light-induced amphiphilic surfaces. *Nature* **1997**, *388*, 431–432. [[CrossRef](#)]
6. Lin, H.; Ouyang, M.; Chen, B.; Zhu, Q.; Wu, J.; Lou, N.; Dong, L.; Wang, Z.; Fu, Y. Design and fabrication of moth-eye subwavelength structure with a waist on silicon for broadband and wide-angle anti-reflection property. *Coatings* **2018**, *8*, 360. [[CrossRef](#)]

7. Loh, J.Y.Y.; Kherani, N. Design of nano-porous multilayer antireflective coatings. *Coatings* **2017**, *7*, 134. [[CrossRef](#)]
8. Drelich, J.; Chibowski, E.; Meng, D.D.; Terpilowski, K. Hydrophilic and superhydrophilic surfaces and materials. *Soft Matter* **2011**, *7*, 9804–9828. [[CrossRef](#)]
9. Wang, P.; Kobiuro, K. Ultimately simple one-pot synthesis of spherical mesoporous TiO₂ nanoparticles in supercritical methanol. *Chem. Lett.* **2012**, *41*, 264–266. [[CrossRef](#)]
10. Kameya, Y.; Yamaki, H.; Ono, R.; Motosuke, M. Fabrication of micropillar TiO₂ photocatalyst arrays using nanoparticle-microprinting method. *Mater. Lett.* **2016**, *175*, 262–265. [[CrossRef](#)]
11. Kameya, Y. Wettability modification of polydimethylsiloxane surface by fabricating micropillar and microhole arrays. *Mater. Lett.* **2017**, *196*, 320–323. [[CrossRef](#)]
12. Taflove, A.; Hagness, S.C. *Computational Electrodynamics: The Finite-Difference Time-Domain Method*, 3rd ed.; Artech House: Norwood, MA, USA, 2005.
13. Chattopadhyay, S.; Huang, Y.F.; Jen, Y.J.; Ganguly, A.; Chen, K.H.; Chen, L.C. Anti-reflecting and photonic nanostructures. *Mater. Sci. Eng. R* **2010**, *69*, 1–35. [[CrossRef](#)]
14. OptiFDTD. Available online: <https://optiwave.com/optifdtd-overview/> (accessed on 14 August 2019).
15. Griffiths, D.J. *Introduction to Electrodynamics*, 4th ed.; Cambridge University Press: Cambridge, UK, 2017.
16. Kameya, Y. Kinetic Monte Carlo simulation of nanoparticle film formation via nanocolloid drying. *J. Nanopart. Res.* **2017**, *19*, 214. [[CrossRef](#)]
17. Drelich, J. Guidelines to measurements of reproducible contact angles using a sessile-drop technique. *Surf. Innov.* **2013**, *1*, 248–254. [[CrossRef](#)]
18. Marmur, A.; Volpe, C.D.; Siboni, S.; Amirfazli, A.; Drelich, J.W. Contact angles and wettability: towards common and accurate terminology. *Surf. Innov.* **2017**, *5*, 3–8. [[CrossRef](#)]
19. Wang, H. From contact line structures to wetting dynamics. *Langmuir* **2019**, *35*, 10233–10245. [[CrossRef](#)] [[PubMed](#)]
20. Allred, T.P.; Weibel, J.A.; Garimella, S.V. A wettability metric for characterization of capillary flow on textured superhydrophilic surfaces. *Langmuir* **2017**, *33*, 7847–7853. [[CrossRef](#)] [[PubMed](#)]



© 2019 by the authors. Licensee MDPI, Basel, Switzerland. This article is an open access article distributed under the terms and conditions of the Creative Commons Attribution (CC BY) license (<http://creativecommons.org/licenses/by/4.0/>).